Nonresonant coherent amplitude transfer in attosecond four-wave-mixing spectroscopy

James D. Gaynor , ^{1,2} Ashley P. Fidler, ^{3,1,2} Yuki Kobayashi , ^{1,4} Yen-Cheng Lin , ^{1,2} Clare L. Keenan , ⁵ Daniel M. Neumark, 1,2,* and Stephen R. Leone 1,2,6,† ¹Department of Chemistry, University of California, Berkeley, California 94720, USA ²Chemical Sciences Division, Lawrence Berkeley National Laboratory, Berkeley, California 94720, USA ³Department of Chemistry, Princeton University, Princeton, New Jersey 08544, USA ⁴SLAC National Accelerator Laboratory, 2575 Sandhill Road, Menlo Park, California 95024, USA ⁵Department of Chemistry, University of Chicago, Chicago, Illinois 60637, USA ⁶Department of Physics, University of California, Berkeley, California 94720, USA

5

10

15

18

20

21

22

23

24

26

27

30

38

(Received 22 November 2022; accepted 14 February 2023; published xxxxxxxxxx)

Attosecond four-wave mixing (FWM) spectroscopy using an extreme ultraviolet (XUV) pulse and two noncollinear near-infrared (NIR) pulses is employed to measure Rydberg wave packet dynamics resulting from XUV excitation of a 3s electron in atomic argon into a series of autoionizing $3s^{-1}$ np Rydberg states ~ 29 eV. The emitted signals from individual Rydberg states exhibit oscillatory structure and persist well beyond the expected lifetimes of the emitting Rydberg states. These results reflect substantial contributions of longer-lived Rydberg states to the FWM emission signals of each individually detected state. A wave packet decomposition analysis reveals that coherent amplitude transfer occurs predominantly from photoexcited $3s^{-1}(n+1)p$ states to the observed $3s^{-1}$ np Rydberg states. The experimental observations are reproduced by time-dependent Schrödinger equation simulations using electronic structure and transition moment calculations. The theory highlights that coherent amplitude transfer is driven nonresonantly to the $3s^{-1}np$ states by the NIR light through $3s^{-1}(n+1)s$ and $3s^{-1}(n-1)d$ dark states during the FWM process.

detected.

DOI: 10.1103/PhysRevA.00.003500

I. INTRODUCTION

Rydberg wave packets are nonstationary states composed of a coherently phased superposition of stationary Rydberg eigenstates. These states are typically well characterized in noble gases, lending them well to systematic investigation. Rydberg state lifetimes are expected to scale by $(n^*)^3$, where the effective principal quantum number $n^* = n - \delta$ accounts for the quantum defect δ ; this follows from established rules for the oscillator strengths of autoionizing states in a Rydberg series [1-3]. Thus, Rydberg series in atomic gases can be used to investigate the evolution of Rydberg wave packets following the broadband excitation of a coherent superposition of well-defined stationary eigenstates. Recent interest in using Rydberg atoms in quantum simulators by coherently manipulating core electrons of atoms while they exist in excited Rydberg states underscores the importance of precisely measuring coherent interactions among autoionizing Rydberg states [4]. The ability to prepare and manipulate quantum superposition states coherently, affecting their individual components and time-dependent evolution, has long been sought after to develop new quantum technologies [5]. One key aspect of interpreting quantum coherences is precisely understanding how information about the superposition

Using broadband attosecond light pulses at extreme ultraviolet (XUV) photon energies produced in tabletop optics laboratories, one can generate a coherent electronic wave packet comprising a superposition of multiple Rydberg states. The evolution of these coherent dynamics may then be followed with attosecond and few-femtosecond temporal resolution owing to the ultrashort pulse durations that are now routinely available [6]. Attosecond four-wave mixing (FWM) spectroscopy is a powerful new means of measuring ultrafast dynamics in atomic and molecular systems that are excited by such broadband XUV attosecond pulses [7–11]. This FWM technique utilizes a noncollinear beam geometry to generate background free XUV emission signals from phase-matched wave-mixing pathways in a sample. Recent attosecond FWM studies have shown that accurate lifetimes of highly excited individual states are directly obtainable in the time domain for a few specific cases. For example, the autoionization lifetimes of the $4p^{-1}6d$, $4p^{-1}7d$, and $4p^{-1}8d$ Rydberg states in gaseous Kr were directly characterized by Fidler et al. [12] in agreement with frequency-domain literature values. Lin et al. [13] measured the few-femtosecond lifetimes of two vibrational levels in gaseous O_2 in the $3s\sigma_g$ Rydberg series converging to the O_2^+ c state \sim 21 eV, revealing an interplay between electronic autoionization rate and internuclear distance. In a study of NaCl with Na⁺ $L_{2,3}$ -edge excitation, Gaynor

et al. [14] identified and characterized the few-femtosecond

lifetimes of several atomiclike core excitons that are highly

is encoded in the reporting states from which a signal is

46

47

49

50

51

53

54

57

58

59

62

63

66

67

^{*}dneumark@berkeley.edu †srl@berkeley.edu

114

117

118

120

121

122

123

124

125

126

127

129

130

131

133

134

135

137

138

139

141

142

143

145

146

147

148

150

151

152

153

154

155

156

159

160

161

163

164

165

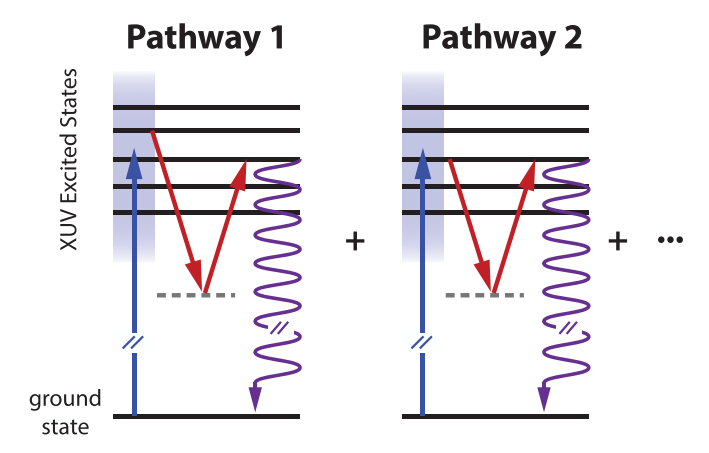


FIG. 1. Multiple-pathway interference schematic for tracking quantum coherences. A broadband attosecond extreme ultraviolet (XUV) pulse excites a large superposition of states, creating a wave packet. The wave packet can then evolve and be affected by consequent light-matter interactions. The detected emission from a single state may contain information from multiple pathways that end in the same final emitting state. The amplitudes and time scales of the measured dynamics can be influenced by each light-matter coupling.

localized about the Na⁺ in the ionic solid. In some cases, the accurate time-domain retrieval of dynamics using attosecond FWM spectroscopy can be known or assumed to be through resonant transitions between XUV-excited bright states and nearby dark states driven by few-cycle near-infrared (NIR) pulses. However, the FWM process can involve optical transitions between multiple excited states, which may occur resonantly or nonresonantly, and the origin of the FWM signal from each individual state may not arise from the particular observed state. An accurate understanding of time-dependent coherent dynamics in atomic and molecular systems requires careful consideration of each light-matter interaction involved in the FWM experiment [15,16].

82

86

87

88

102

103

106

107

108

Figure 1 illustrates how a broad bandwidth of XUV-excited states, such as in a Rydberg wave packet, is monitored in attosecond FWM spectroscopy. The blue shaded region indicates the coherent excitation of many stationary eigenstates by the broadband XUV light pulse represented by the blue arrow, and the two red arrows reflect consequent time-controlled light-matter interactions between the XUV-excited states and nearby dark states that are driven by few-cycle NIR pulses. The two depicted pathways show that two or more different excited states within the wave packet can couple directly to the same XUV bright state from which the signal is emitted. As explored in this paper, this mechanism can lead to the amplitudes and time scales from otherwise unexpected states influencing or even dominating the dynamics of the FWM emission signals.

In this paper, attosecond FWM spectroscopy is used to study Rydberg wave packet dynamics arising from single 3s electron excitations in gaseous Ar, accessing the $3s^{-1}3p^6np$ (^{1}P) series of autoionizing Rydberg states that converge to the $3s^{-1}3p^6(^{2}S_{1/2})$ level of Ar $^{+}$ at 29.24 eV [17,18]. A broadband attosecond XUV pulse initiates a coherent superposition of these $3s^{-1}np$ Rydberg states ($n \ge 4$), creating the Rydberg wave packet. Then two noncollinear

few-cycle NIR pulses probe the evolution of the Rydberg wave packet. The light-matter interactions complete a phase-matched wave-mixing process, producing an XUV emission from each of the $3s^{-1}$ np Rydberg states that is spectrally and temporally resolved. Thus, the wave packet dynamics are projected onto each $3s^{-1}$ np Rydberg state emission. As illustrated in Fig. 1, the observed time-dependent FWM emission from each Rydberg state contains information about how the amplitudes of the multiple states in the initial Rydberg wave packet are transferred through the second and third light-matter interactions driven by the NIR pulses.

A comprehensive analysis of coherent superpositions created by the excitation of an Ar $3s^{-1}np$ Rydberg wave packet \sim 29 eV is presented. The experimental measurements are fitted to a wave packet model to extract the amplitude coefficients of the coherent superposition responsible for the time-dependent FWM emission from individual $3s^{-1}np$ Rydberg eigenstates. Calculations using the time-dependent Schrödinger equation (TDSE) support the measurements and wave packet modeling to elucidate the coherent amplitude transfer that occurs during the few-cycle NIR pulse interactions, resulting in the set of coherent oscillations observed in the detected individual state emissions. The results indicate that the coherent decay signals from $3s^{-1}np$ states are dominated by their coupling to longer-lived $3s^{-1}(n+1)p$ states created by the XUV excitation pulse and that this coupling occurs via nonresonant amplitude transfer through the optically dark $3s^{-1}(n+1)s$ and $3s^{-1}(n-1)d$ states driven by the NIR pulses. Moreover, each emitting $3s^{-1}np$ state displays strong quantum beating, primarily between itself and the $3s^{-1}(n+1)p$ state, with minor components from other states. Overall, the Rydberg series measurements reported here act as a vehicle for elucidating the role of nonresonant coherent amplitude transfer in attosecond FWM spectroscopy.

II. RESULTS AND ANALYSIS

A. Attosecond FWM spectra of Ar Rydberg wave packets

The apparatus and technique have been described previously [12,14]. Briefly, the output of a Ti:sapphire laser (Femtopower, 1 kHz repetition rate, 1.7 mJ/pulse, 22 fs, 780 nm) is spectrally broadened in a stretched hollow core fiber compressor (Few-Cycle Inc.) and temporally compressed using a combination of seven chirped mirror pairs (Ultrafast Innovations, PC70), fused silica wedge pairs, and a 2-mm-thick ammonium dihydrogen phosphate crystal. This yields pulses of sub-6 fs pulse durations with spectra spanning 550–950 nm and $\sim\!600\,\mu\text{J/pulse}$ energies. The beam is then split by a 75:25 (R:T) beam splitter in a Mach-Zender interferometer to separate the NIR driving pulse used to create the XUV pulse by high harmonic generation (HHG) from the pulse used to generate the two noncollinear NIR beams.

Attosecond pulses of XUV radiation in the 25–45 eV range are produced by HHG in Kr (\sim 4 Torr backing pressure). A 150-nm-thick Al foil attenuates the copropagating NIR driving field from the newly generated XUV pulse. The transmitted XUV pulse is refocused by a gold-coated toroidal mirror through an annular mirror into a 1 mm pathlength gas cell for the sample, in which Ar flows out of the laser

170

171

172

174

175

177

178

179

180

181

182

183

186

187

188

190

191

194

195

196

198

199

200

203

204

205

206

207

210

211

212

213

214

215

216

219

220

221

222

223

224

225

entrance and exit pinholes at a backing pressure of 14 Torr. The remaining NIR pulse in the other arm of the Mach-Zender interferometer is delayed relative to the XUV beam using a piezoelectric translation stage, and this beam is then further split with a 50:50 beam splitter to create the two NIR pulses for use in the wave-mixing experiment. The relative temporal delay between the two NIR pulses is further controlled using a second piezoelectric translation stage. The two NIR beams are focused and routed through the vacuum chamber to the sample cell to overlap with the XUV pulse spatially and temporally. The two NIR beams are vertically arranged, one above and one below the XUV beam. The interaction of all three beams with the sample produces the phase-matched background free FWM signal.

The NIR pulse envelope is estimated to be 5.6 fs from the rise time of the Ar $3s^{-1}4p$ autoionization signal measured by attosecond transient absorption (ATA). The emitted XUV signals are filtered using another 150 nm thick Al foil, then spectrally dispersed in the horizontal plane with a flat field grating and recorded using an x-ray charge-coupled device (CCD) camera. In addition to the background free wave-mixing signals, there are ATA signals that copropagate with the XUV beam. The wave-mixing signals can be isolated from the ATA signal and residual XUV beam and then further optimized using a vertically translatable camera mount that allows for the unwanted ATA signals and XUV beam to be translated off the CCD imaging area.

The transient FWM spectrum of the Ar $3s^{-1}np$ Rydberg wave packet is shown in Fig. 2(a) with temporal lineouts shown as solid lines in Fig. 2(b). Time-dependent emissions from the $3s^{-1}5p-9p$ Rydberg states appear as horizontal features in Fig. 2(a). Signatures from the coherent superposition of Rydberg states are prominent in the FWM signals, manifested as strong intensity oscillations in the emissions from each $3s^{-1}np$ Rydberg state. Clear variations exist in the coherent oscillation periodicity and modulation depth for $3s^{-1}$ np emissions of different principal quantum number. In general, the oscillations have a larger modulation depth and a lower frequency as n increases. The decay times of the $3s^{-1}np$ emissions increase with n, in qualitative agreement with the well-known trend in autoionization lifetimes. However, the measured decay time of each $3s^{-1}np$ emission is substantially longer than expected from frequency-domain linewidth measurements [17,19,20] and calculations [21] found in the literature for that state. For example, the $3s^{-1} 5p$ and $3s^{-1} 6p$ state linewidths obtained from synchrotron photoabsorption experiments are 28.2 and 12.6 meV, respectively, corresponding to lifetimes of 23.3 and 52.2 fs [17,19]. For comparison, single exponential decay functions with the decay rate corresponding to the frequency-domain line widths for the $3s^{-1} 5p$ and $3s^{-1}$ 6p Rydberg states are shown in Fig. 2(b) as dashed blue and dashed red lineouts, respectively. The experimental temporal lineouts of the $3s^{-1}5p$ (blue) and $3s^{-1}6p$ (red) states in Fig. 2(b) decay on \sim 50 and \sim 150 fs time scales, respectively.

The discrepancy between the frequency-domain linewidths and the time-domain FWM decays in Fig. 2(b) along with the pronounced quantum beating conveys that the observed Ar $3s^{-1}np$ Rydberg series FWM emissions exhibit more complex dynamics than a one-to-one mapping of the ini-

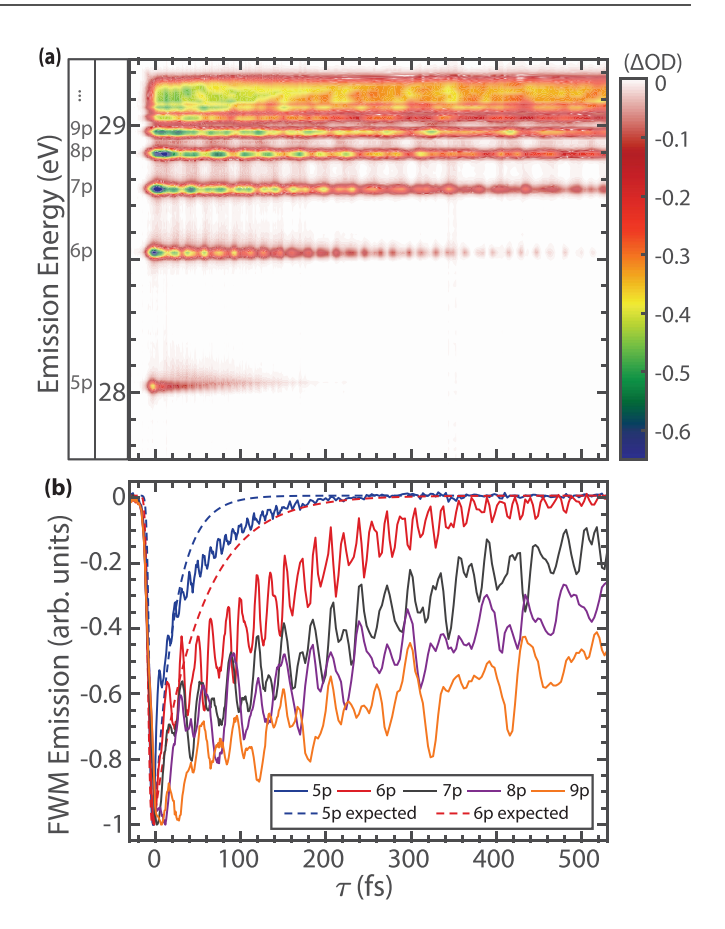


FIG. 2. Strong coherent oscillations in transient four-wave mixing (FWM) spectra of Ar $3s^{-1}np$ Rydberg series. (a) The transient FWM spectra of the autoionizing Ar $3s^{-1}np$ Rydberg series. (b) Temporal traces taken at the peaks of various Rydberg state emissions to see the temporal oscillations more clearly. The solid lineouts in (b) correspond to experimentally measured traces, while the dashed blue and dashed red traces are simulated single exponential decay functions with the decay rates specified from frequency-domain linewidth measurements of 23.3 fs for the 5p and 52.2 fs for the 6p, respectively.

tial Rydberg wave packet excited by the attosecond XUV pulse. Previous work [12] has shown this one-to-one mapping can occur when the NIR interactions are resonant with XUV dark states during V- or Λ -type FWM pathways. To better understand the detected FWM emission from the Ar $3s^{-1}np$ Rydberg wave packet, the features in Fig. 2 are decomposed into the constituent eigenstates in the superposition by determining their relative amplitudes and phase.

231

232

234

235

236

239

240

243

244

245

Analysis of the $3s^{-1}$ 5p emission is presented in Figs. 3(a)–3(d), and the $3s^{-1}$ 6p emission is shown in Figs. 3(e)–3(h). The decay of the nth Rydberg eigenstate is represented as $\psi_n(\omega_n, \Gamma_n, t) = -\exp(i\omega_n t - \frac{\Gamma_n}{2}t)$, while $\Psi(t) = \sum_n A_n \times \psi_n(\omega_n, \Gamma_n, t)$ is the coherent superposition of all Rydberg eigenstates. Here, ω is the Rydberg state energy, Γ is the autoionizing linewidth, and $A_n = a_n \exp(i\phi_n)$ are the complex superposition coefficients with amplitudes a_n and phase ϕ_n . The emitted FWM signal reports on the dynamics of the Rydberg wave packet, and the intensity of the emitted electric field during the FWM process is detected

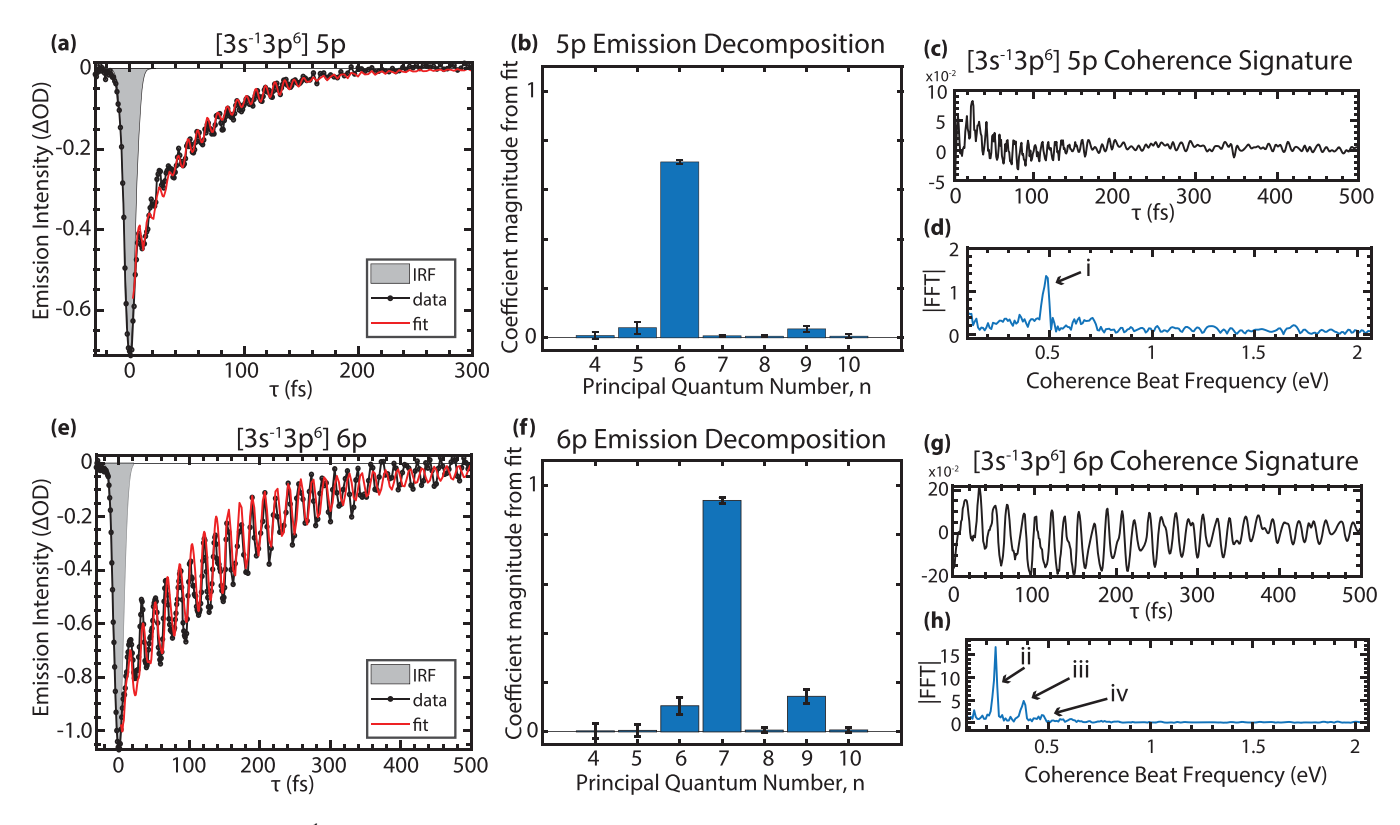


FIG. 3. Extracting the $3s^{-1}np$ state amplitudes composing the Rydberg wave packet through four-wave mixing emission. The wave-mixing signal of the $3s^{-1}5p$ signal is analyzed in (a)–(d), and the $3s^{-1}6p$ signal is analyzed in (e)–(h). The signals are first fit to the wave packet model described in the text (a) and (e). The coefficient amplitudes a_n of each component Rydberg state in the wave packet is plotted as obtained from the fit (b) and (f) with the error bars representing the 95% confidence interval of the amplitudes. The exponential decay components from the fit are subtracted to isolate the coherent oscillations in the wave-mixing signals (c) and (g), and then the oscillations are Fourier transformed to identify the primary coherence components in the signals (d) and (h). Peaks labeled i–iv are discussed further in the text.

experimentally. The experimental data are fit to $|\Psi(t)|^2$ using this model; to fit the FWM emission traces, the Rydberg state energies were initially set to literature values and allowed to float by ± 10 meV to match more closely the 11 meV experimental resolution of our spectrometer. The fits in Fig. 3 were obtained by including the $4 \le n \le 10$ members of the $3s^{-1}$ np series. See Appendix A for further information on the fitting procedure.

240

252

253

254

255

256

257

258

261

262

263

265

267

268

269

270

271

The emitted FWM signal reflects the dynamics of the coherent superposition resulting from the initial XUV-prepared Ar $3s^{-1}\,np$ Rydberg wave packet being reshaped from two NIR light-matter interactions. It is important to note the difference between the initial Rydberg wave packet prepared by the XUV pulse and the coherent superposition that generates the FWM emission signal. The detected coherence signal results from probing the initial XUV-prepared Rydberg wave packet with the two NIR light-matter interactions that project part of the initial Rydberg wave packet onto each final Rydberg state, which then emits a FWM signal.

As shown in Figs. 3(a) and 3(e), very good agreement between the model and the experimental data is achieved for the $3s^{-1}5p$ and $3s^{-1}6p$ emissions, giving R^2 goodness of fit parameters of 0.99 and 0.96, respectively. The emitted coherence dynamics observed in the $3s^{-1}5p$ and $3s^{-1}6p$ emissions are then elucidated by plotting the a_n coefficients for all eigenstates in Figs. 3(b) and 3(f). Interestingly,

emission from the $3s^{-1}5p$ state is dominated by the character of the $3s^{-1}6p$ state; similarly, the $3s^{-1}6p$ emission is dominated by the $3s^{-1}7p$ state. This trend also holds for the $3s^{-1}7p$ emission, although the fit is worse for higher n Rydberg states, as neighboring states are energetically closer; see Appendix A for 7p fitting.

275

276

277

278

279

280

283

284

287

288

289

291

292

293

296

297

The FWM intensity oscillations characterizing the coherent superposition are directly analyzed by subtracting the multiexponential decay that arises from the fits as the diagonal $|A_n\psi_n|^2$ terms. The experimental coherence signatures of the $3s^{-1} 5p$ and $3s^{-1} 6p$ emissions are isolated in Figs. 3(c) and 3(g), along with their Fourier transforms in Figs. 3(d) and 3(h), respectively. These signatures reflect the cross terms of the type $(A_n\psi_n)(A_m\psi_m)$, where $n\neq m$. The most intense oscillations of the np emission, e.g., peak i at 0.49 eV and peak ii at 0.24 eV in Figs. 3(d) and 3(h), respectively, occur at the beat frequency corresponding to the energy difference between the (n+1)p and the np Rydberg states. These respective energy differences are consistent with the 0.50 eV separation of the $3s^{-1}5p$ and $3s^{-1}6p$ states and with the 0.24 eV separation of the $3s^{-1}6p$ and $3s^{-1}7p$ states as measured in our spectrometer. We note that the 5.6 fs duration of the instrument response may limit the experimental resolution of the coherent modulation depth for superposition states with energetic separation >0.7 eV (5.9 fs). However, this does not alter the analysis, which is primarily determined by the

326

329

330

333

334

337

338

341

342

345

346

349

350

351

353

354

358

359

361

362

363

367

370

371

374

375

378

379

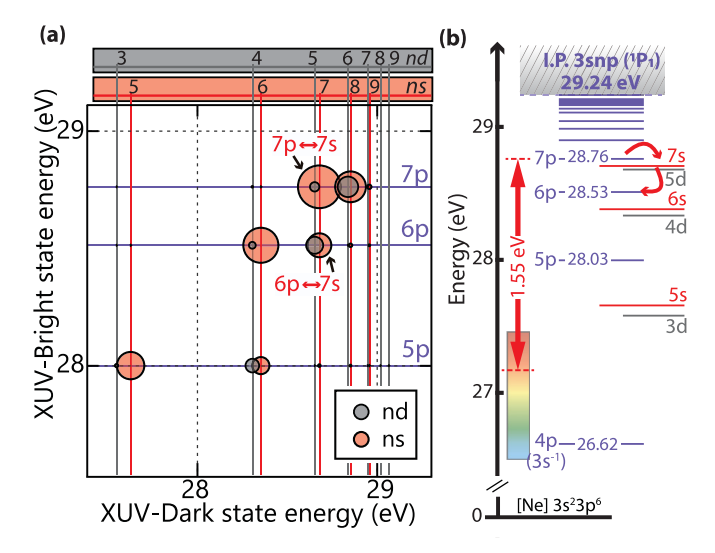


FIG. 4. Calculated oscillator strengths and energy level diagram for extreme ultraviolet (XUV)-bright and dark states. The energies of the $3s^{-1}np$, $3s^{-1}ns$, and $3s^{-1}nd$ Rydberg state with respect to the [Ne] $3s^2 3p^6$ ground state of Ar are shown in (a). The XUVallowed $3s^{-1}$ np states are plotted on the vertical axis with purple grid lines, and the XUV-forbidden $3s^{-1}$ ns and $3s^{-1}$ nd states are plotted on the horizontal axis with pink and gray lines, respectively. The oscillator strengths for the $3s^{-1}$ $np \leftrightarrow 3s^{-1}$ $ns/3s^{-1}$ nd transitions are represented by the size of the circles; the position of the circle in the two-dimensional plot specifies the transition. An energy level diagram of relevant states in Fig. 3 is shown in (b). The center energy and bandwidth of the near-infrared (NIR) pulses is shown with respect to the $3s^{-1}7p$ state to highlight the nonresonant condition probed in the experiment (NIR bandwidth is represented by the rainbow-colored box). See text for discussion of the example pathway highlighted in this figure.

lifetimes of the decaying Rydberg states, rather than the depth of modulation.

300

301

302

304

305

309

310

313

314

316

317

318

319

It is clear from the analysis in Fig. 3 that the NIR wave-mixing pulses drive pathways that transfer amplitude from the (n+1)p states of the Rydberg wave packet to the np states that produce FWM emission. There are additional superposition components of smaller magnitude in Figs. 3(d) and 3(h). Peak iii appears at 0.38 eV, in good agreement with the experimentally measured 0.37 eV energy difference between the $3s^{-1}6p$ and $3s^{-1}8p$ Rydberg states. Although weak, peak iv appears at 0.47 eV and is assigned to interfering contributions between the $3s^{-1}5p$ and $3s^{-1}6p$ coherence and the $3s^{-1}6p$ and $3s^{-1}9p$ coherence, both of which are expected at 0.45 eV. As discussed below in Fig. 4, consideration of oscillator strengths between XUV bright and dark states that are all far off-resonant with the NIR pulses provide a rationale for why certain states contribute more than others in this specific case.

B. Calculated oscillator strengths: A quantum roadmap

In this section, the experimentally observed coherence dynamics are explored theoretically to understand the physical origins of the coherence signatures discussed above with the goal of understanding more clearly how the NIR pulses complete the FWM pathways to produce the emitted signals. To achieve this, the oscillator strengths between the bright and dark states are calculated (Fig. 4), and the timedependent emissions of an Ar $3s^{-1}np$ Rydberg wave packet are simulated and analyzed (Fig. 5). The energies of the Ar ground, $3s^{-1} np \ (4 \le n \le 9)$, $3s^{-1} ns \ (4 \le n \le 9)$, and $3s^{-1}$ nd $(3 \le n \le 9)$ states are calculated using the Cowan atomic structure code [22]. See Appendix B for further details on electronic structure calculations. The oscillator strengths between the XUV-allowed $3s^{-1}np$ states and the XUVforbidden $3s^{-1}$ ns and $3s^{-1}$ nd states are shown in Fig. 4(a) through the relative area of the colored circles. For example, the pink circle in the bottom left reflects the oscillator strength for the transition between the $3s^{-1}5p$ and $3s^{-1}5s$ states and is calculated as 0.494. Similarly, the calculated oscillator strength for the $3s^{-1}5p$ to $3s^{-1}6s$ transition is 0.301. Table I lists the oscillator strengths for the principal transitions shown in Fig. 4(a). The oscillator strengths for the other transitions not listed in the table are typically orders of magnitude smaller; see Appendix B for a complete list of calculated oscillator strengths.

Collectively, Fig. 4(a) and Table I show that the largest oscillator strengths are for transitions where, first, the angular orbital momentum quantum number reduces by one (e.g., 7p to 7s in the first column), followed by strong oscillator strengths for transitions where the principal quantum number also changes (e.g., 6p to 7s in the second column). A representative pathway connecting $3s^{-1}7p$ character with the $3s^{-1}6p$ state is pointed out with arrows and labels in Fig. 4(a) and with red curved arrows in Fig. 4(b). This pathway demonstrates that the $3s^{-1} 7p$ excitation can connect to the $3s^{-1} 7s$ dark state with the first NIR interaction, followed by the transition to the $3s^{-1}6p$ bright state with the second NIR interaction. In this way, Fig. 4(a) serves as a map of the quantum transition pathways that result in the observed coherence signatures and the extended decay times of the Ar $3s^{-1}np$ Rydberg states in Fig. 2. Specifically, the results suggest that the (n+1)s and (n-1)d states are the dominant XUV-forbidden states connecting the np and (n+1)pstates during the FWM process. When the Rydberg wave packet dynamics are projected back onto the $3s^{-1}np$ states by the XUV \pm NIR₁ \pm NIR₂ pulse sequence, the enhanced (n+1)p character extends the coherent wave packet dynamics observed in the FWM signal decay time beyond what is expected from the individual $3s^{-1}np$ Rydberg states. These calculations are consistent with the experimental observations shown in Fig. 3. Interestingly, as the energy level diagram in Fig. 4(b) shows, the observed FWM transition pathways are highly nonresonant for the NIR pulses. The energy separations between identified states involved in the wave-mixing pathways span 0.05-0.35 eV, whereas the NIR pulse spectrum spans 1.23-2.25 eV.

To confirm the origin of the time-dependent behavior measured in the FWM experiment, the transient response of the argon atoms is simulated by numerically solving the TDSE where the transition dipole moments between the calculated $3s^{-1}np$, $3s^{-1}ns$, and $3s^{-1}nd$ states are explicitly included. The results are shown in Fig. 5; see Appendices for TDSE simulation details. The TDSE simulation in Fig. 5(a) shows prominent coherences, and the beat frequencies are identified by Fourier transform analysis in Fig. 5(b). The Fourier

384

387

388

389

391

392

393

395

396

397

399

400

401

403

404

405

407

408

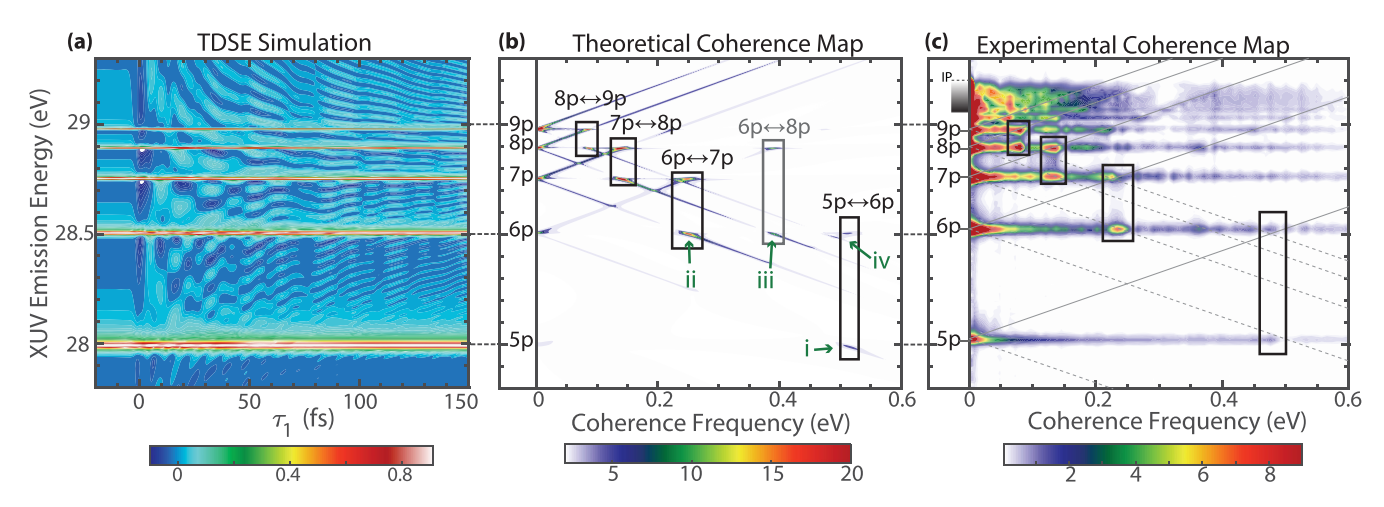


FIG. 5. Theoretical and experimental coherence maps of the Rydberg wave packet. (a) A simulation of the Ar $3s^{-1}$ np dipole emission by solving the time-dependent Schrödinger equation captures the extended decay times observed in the wave-mixing experiments. (b) The Fourier transform of the simulated signal further matches the coherent oscillatory signatures observed as the Rydberg wave packet propagates. The experimental wave-mixing spectrum from Fig. 2(a) is Fourier transformed for comparison to the result in (b). The solid black boxes in (b) and (c) highlight the retrieved beat frequencies that match the energy differences between the np and (n+1)p Rydberg states, consistent with the wave packet decomposition trends shown in Figs. 3(b) and 3(f). The gray box in (b) shows an additional coherence contribution relevant for the $3s^{-1}$ 6p emission, as discussed in the text. Peaks i–iv from the experimental analysis in Figs. 3(d) and 3(h) are labeled in green.

components from the TDSE simulation highlight the influence of the oscillator strengths calculated in Fig. 4(a) through the dynamics. For comparison with theory, the experimental FWM spectrum in Fig. 2(a) has also been Fourier transformed over the XUV-NIR time delay (τ_1) , which is given in Fig. 5(c). We note that the experimental coherence peaks lie on top of strong features at very low frequencies that approach 0 eV due to the underlying exponential decay dynamics. The noise level in Fig. 5(c) is greater than the FFT analyses in Figs. 3(d) and 3(h) because the underlying multiexponential decay components cannot be removed globally to enable the enhanced resolution FFT analysis shown in Fig. 3.

The black outlined boxes in Fig. 5(b) group the beat frequencies of the coherences involving the np and (n+1)p states. The gray box shows the additional $6p \leftrightarrow 8p$ coherence viewed in the 6p emission. Peaks i–iv, as observed in the experimental analysis of Figs. 3(d) and 3(h), are labeled in green in the theoretical coherence map of Fig. 5(b), providing theoretical confirmation of the identified coherences and explanation. Peak i is present in the theoretical 5p emission at 0.50 eV coherence frequency and 27.99 eV XUV emission energy. Peak ii is observed in the theoretical 6p emission at 0.24 eV coherence frequency and 28.51 eV XUV emission energy. Peak iii appears at 0.38 eV coherence frequency and 28.51 eV. The two expected contributions to peak iv are present in the theoretical 6p emission; the $5p \leftrightarrow 6p$ coherence

TABLE I. Calculated oscillator strengths for NIR-driven principal transitions (arb. units).

np	(n)s	(n+1)s	(n-2)d	(n-1)d
5 <i>p</i>	0.494	0.301	0.049	0.238
6 <i>p</i>	0.637	0.429	0.103	0.305
7 <i>p</i>	0.776	0.557	0.158	0.368

is observed at 0.50 eV, and the $6p \leftrightarrow 9p$ coherence feature appears at 0.46 eV.

409

410

411

413

414

417

418

420

421

422

423

424

425

426

427

428

429

430

431

433

434

435

437

438

439

441

III. DISCUSSION

The coherent nature of the dynamics involving many Rydberg eigenstates is on full display in the presented experiments and accompanying theory, as the oscillatory intensity of the np FWM emission extends much longer than expected. For example, the $3s^{-1}5p$ emission has visible oscillations out to \sim 150–200 fs even though the 3s⁻¹ 6p autoionization lifetime is 52.2 fs. Although higher n members of the Rydberg series make up small portions of the amplitude distribution in the fitted FWM emissions, they are still part of the coherent superposition and thus exert influence over its time dependence. The agreement between the experimental FWM signals and the simulated results shows that the detected coherent wave packet dynamics are largely driven by the transition dipoles of the NIR coupled states in the excited $3s^{-1}np$ Ar system itself, even though there are no XUV-forbidden states $(3s^{-1} ns/d)$ to complete the wave-mixing pathways lying within the NIR bandwidth. By contrast, previous FWM experiments on the Kr $4s^2 4p^5 nl$ autoionizing Rydberg series used NIR-resonant $4p^{-1}np$ states to measure $4s^2 4p^5 nl$ state lifetimes that matched frequency-domain lifetime predictions [12]. Theoretical investigations of similar off-resonant conditions in ATA spectroscopy also show that the dynamics can be governed largely by transition dipole moments and coherent dephasing rather than by population transfer and relaxation, as occurs when on resonance [23].

The results in this paper may be considered through the lens of wave packet reshaping where coherent amplitude transfer, which occurs through nonresonant NIR light-matter interactions, changes the amplitude coefficients in the superposition of the detected coherence in relation to the initial

504

505

508

509

510

512

513

514

517

518

521

522

524

525

526

527

531

444

445

448

451

452

453

454

456

457

460

461

462

464

465

468

469

470

473

474

477

478

479

480

481

485

486

487

489

490

493

494

495

497

498

499

XUV-excited Rydberg wave packet. These FWM studies of Ar Rydberg wave packets show that a systematic alteration of autoionization events is possible that is intrinsic to the system itself after a Rydberg wave packet is launched. As the amplitude distributions show from the wave packet decomposition in Fig. 3, the off-resonant NIR interactions have the effect of redistributing or transferring amplitude among the Rydberg eigenstates that compose the coherent superposition, i.e., from the $3s^{-1}(n+1)p$ states to the $3s^{-1}np$ states. Importantly, the nature of the coherent amplitude transfer relies upon the transition dipole moments connecting $3s^{-1} np$, $3s^{-1}$ ns, and $3s^{-1}$ nd states within the excited state system. It is also significant that the FWM emission decays of the autoionizing np states are extended here rather than shortened with respect to their literature line-width values. Other time-dependent wave packet studies have shown detected coherence lifetimes decaying on the time scale of the shorterlived components in the superposition [24]. ATA spectroscopy has been used to measure Ar $3s^{-1} 4p$ and $3s^{-1} 5p$ decay times consistent with frequency domain literature due to NIR coupling with continuum states or, for the $3s^{-1}4p$ state, through resonant dark states accessed by one NIR photon [25]. The nonresonant NIR-coupled pathways in this attosecond FWM experiment show that the transition dipole moments connecting the (n+1)s and (n-1)d dark states to the np states maintain the coherence in the detected superposition, allowing for the *np* state to be detected through its quantum interference with the (n+1)p state long after its autoionization lifetime. The coherent amplitude transfer dynamic reported here sheds new light on important and complex coherent detection dynamics of autoionizing states that are ultimately governed by electron-electron correlations.

There is longstanding interest in coherently controlling excited state processes with systems ranging in complexity from prototypical atomic Rydberg wave packets [5,26–30] to mixed electronic, vibrational, and rotational wave packets in small molecules [24,31,32]. Often, the approach to controlling wave packet dynamics surrounds the preparation of the coherent superposition using pulse shaping methods with iterative feedback to customize the wave packet composition for particular trajectories. The results in this paper do not go as far as coherent control. Frequency-domain pulse shaping methods have been previously used in the attosecond FWM experiment to analyze the NIR frequency dependence of an attosecond FWM experiment on the Ar $3s^2 3p^5 ns/nd$ autoionizing Rydberg series [33]. In this application the fewcycle NIR light-matter interactions were on resonance with optically dark $3s^2 3p^5 4p$ states, which enabled the isolation of specific wave-mixing pathways from the coherences using the pulse shaper. Other more recent experiments have targeted the $3s^2 3p^5 nf$ autoionizing Rydberg series in Ar in which Rydberg wave packet control is probed through narrower band Raman transitions and using photoelectron-based detection [34]. In contrast, the results presented here provide important insight about the role that nonresonant NIR light-matter interactions can have in coherently transferring amplitude during the attosecond FWM process. More broadly, in this paper, we emphasize the importance of carefully considering the nature of each light-matter interaction and coherence transfer during the probing stages of an initially excited wave packet.

IV. CONCLUSIONS

We have reported attosecond FWM spectra of the Ar $3s^{-1}$ np autoionizing Rydberg series $\sim 27-29$ eV. In this investigation, we highlight the important role of nonresonant NIR light-matter interactions in probing XUV-excited Rydberg wave packets. The reported experiments and analysis reveal a mechanism of coherent amplitude transfer arising from the nonresonant NIR light-matter interactions that explain the detected FWM emission coherence decays. Importantly, in this paper, we identify the specific optically dark (n+1)s and (n-1)d states that are responsible for transferring (n+1)p character to the np states, from which the FWM emissions are detected. This results in the apparent lifetimes of Rydberg states other than the directly observed individual emissions dominating the FWM coherence decays. The overarching importance of a careful consideration of each light-matter interaction in the attosecond FWM process is emphasized in this paper. The insight contributed by this paper also has wide-ranging implications for current work in quantum information science, where the steps of creation, manipulation, and readout of coherent states are crucial to the performance and robustness of future quantum technologies.

ACKNOWLEDGMENTS

Work for this paper was performed by personnel and equipment supported by the Office of Science, Office of Basic Energy Sciences through the Atomic, Molecular and Optical Sciences Program of the Division of Chemical Sciences, Geosciences, and Biosciences of the U.S. Department of Energy at LBNL under Contract No. DE-AC02-05CH11231. J.D.G. is grateful to the Arnold and Mabel Beckman Foundation for

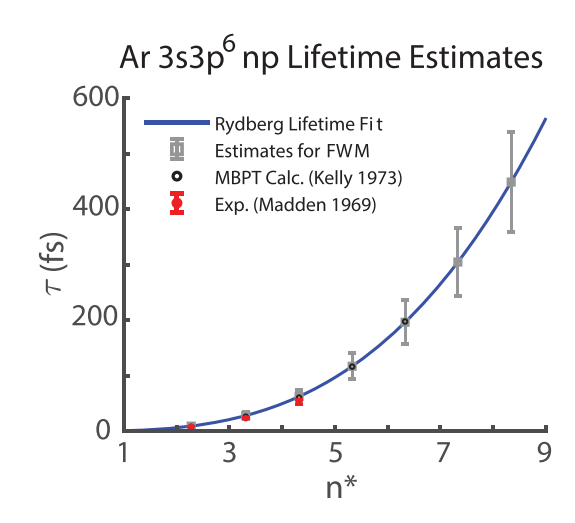


FIG. 6. Determining autoionization lifetimes of higher members (n > 8) of Ar $3s^{-1}$ np autoionizing Rydberg series. The blue fit is used to determine the autoionization lifetime of the higher n members in the wave packet model used to fit the attosecond four-wave mixing (FWM) spectra shown in Fig. 3.

561

563

564

567

568

569

571

572

573

575

576

577

580

583

584

585

534

535

536

538

539

543

544

546

547

550

551

552

553

554

555

556

558

559

FIG. 7. Wave packet model fitting of the Ar $3s^{-1}7p$ lineout. The fit to the experimental data is shown (a), and the extracted amplitude coefficients are shown in (b).

support as an Arnold O. Beckman Postdoctoral Fellow. A.P.F. acknowledges support from the National Science Foundation (NSF) Graduate Research Fellowship Program, and Y.K. and S.R.L. acknowledge NSF Grant No. CHE-1951317 and No. 2243756 for program support that led to the calculational aspect of the research. Y.-C.L. acknowledges financial support from the Taiwan Ministry of Education. Y.K. also acknowledges the support from the Urbanek-Chorodow Fellowship at Stanford University. C.L.K. acknowledges support from the NSF Research Experience for Undergraduates (REU) program Grants No. EEC-1461231 and No. EEC-1852537. The authors are grateful to Dr. Kenneth Schafer and Dr. Mette Gaarde for helpful discussions of nonresonant light matter interactions.

J.D.G., A.P.F., Y.-C.L., C.L.K., D.M.N., and S.R.L. designed the experiments. J.D.G., A.P.F., Y.-C.L., and C.L.K. performed the experiments. J.D.G. performed the data analysis and modeling. Y.K. provided theoretical calculation and simulations. J.D.G. A.P.F., Y.K., Y.-C.L., C.L.K., D.M.N., and S.R.L. discussed the results. J.D.G. wrote the paper.

APPENDIX A: WAVE PACKET MODEL ANALYSIS

The equations used to fit the attosecond FWM lineouts are described in the main text. The 5p and 6p states were sufficiently fit using a wave packet of the $3s^{-1}np$ states where $4 \le n \le 10$, while the 7p state required up to n = 15. The autoionizing Rydberg state energies were obtained from literature values [17,21,35,36]. The autoionizing lifetimes for

TABLE II. $3s^{-1} 5p$ fit; $R^2 = 0.99$.

\overline{n}	a_n	ϕ_n (radians)	$\Gamma_n (\tau_n) (eV)$	τ_n (fs)	ω_n (eV)
4	0.00959	2.752	0.090	7.31	26.61
5	0.04113	2.592	0.029	22.46	27.98
6	0.7137	0.822	0.012	54.47	28.49
7	0.00829	-0.488	0.007	93.60	28.78
8	0.00682	-1.925	0.004	157.00	28.91
9	0.03638	-2.643	0.003	243.80	28.98
10	0.00689	0.212	0.002	359.20	29.03

the $3s^{-1}$ np Rydberg states have been reported in the literature up to n=8. To constrain the autoionizing lifetimes τ for all Rydberg states used in the wave packet model, the lifetimes for the $4 \le n \le 8$ states in the series were compiled from the literature [17,18,21] and fit to the well-known cubic scaling law for autoionizing lifetimes [1–3] $\tau = \tau_0(n-\delta)^3$, where τ_0 is a proportionality constant and δ is the known quantum defect. Using this fit, the higher members of the Rydberg series that are not available in the literature can be included in the analysis in a consistent manner with the known lifetimes of the lower n members. The cubic scaling fit is shown in Fig. 6 for extrapolating higher n member lifetimes.

1. The Ar $3s^{-1}$ 7p lineout fit

As noted in the main text, the wave packet model fitting becomes less robust as the stationary Rydberg eigenstates composing the wave packet become closer in energy, which clearly begins to affect the fitting in the 7p lineout. The 7p lineout is shown in Fig. 7.

2. Fitted parameters of the Ar $3s^{-1}5p$, 6p, and 7p lineouts

The Levenburg-Marquardt algorithm was used in a nonlinear least squares fitting routine using the wave packet model equation given in the main text. The amplitude coefficients a_n were optimized to fit the experimental data by the fitting algorithm, while the autoionizing linewidth (lifetime) $\Gamma_n(\tau_n)$ and eigenstate energy ω_n were initially set to literature-

TABLE III. $3s^{-1} 6p$ fit; $R^2 = 0.96$.

n	a_n	ϕ_n (radians)	$\Gamma_n (\tau_n) (eV)$	τ_n (fs)	ω_n (eV)
4	0.00441	-2.406	0.090	7.31	26.63
5	0.00644	3.142	0.020	33.43	28.00
6	0.1062	0.382	0.009	74.93	28.51
7	0.9393	-0.096	0.005	140.40	28.76
8	0.00753	1.487	0.003	235.30	28.89
9	0.1446	-3.142	0.002	365.80	29.00
10	0.00807	-0.230	0.002	359.20	29.04

TABLE IV. $3s^{-1} 7p$ fit; $R^2 = 0.76$.

n	a_n	ϕ_n (radians)	$\Gamma_n (\tau_n) (eV)$	τ_n (fs)	ω_n (eV)
6	0.00328	-0.9799	0.009	74.9	28.52
7	0.206	-0.8908	0.005	140.4	29.17
8	1.012	-1.143	0.003	235.6	28.74
9	0.037	-0.1997	0.003	243.8	28.88
10	0.2189	1.920	0.001	538.8	29.00
11	0.00540	-0.4899	0.001	550.0	29.02
12	0.01882	-3.139	0.001	1100	29.08
13	0.02858	3.142	0.0004	1499	29.10
14	0.01892	-1.579	0.0004	1700	29.12
15	0.02274	-1.724	0.0003	2400	29.15

obtained values and then constrained with upper and lower boundaries in the fitting algorithm to enable convergence. The autoionizing lifetimes were obtained as described above in Appendix A based on available literature; the eigenstate energies were given upper and lower boundaries separated by 10 meV to approximate the 11 meV instrumental spectral resolution and enable the fitting algorithm to converge effectively. The phase ϕ_n was allowed to float over the range $-\pi$ to π radians during fit optimization (see Tables II–IV).

587

591

592

595

599

600

602

603

605

606

607

608

609

610

611

613

614

As can be seen from the higher member fitted parameters, especially those for $n \ge 8$, the narrow linewidths are too narrow to be spectrally resolved, and they begin to complicate the physical accuracy of the fit.

APPENDIX B: COMPUTATIONAL METHODS

1. TDSE simulation

The core-level time-dependent absorption response of argon atoms is simulated by numerically solving the TDSE for the discrete electronic levels:

$$i\frac{\partial}{\partial t}c_n(t) = \epsilon_n - \frac{i\Gamma_n}{2} - \sum_{m \neq n} d_{n,m}E(t).$$
 (B1)

In Eq. (B1), $c_n(t)$ is the complex coefficient for the nth electronic state, ϵ_n is the state energy, Γ_n is the autoionization lifetime of the core-excited states obtained in the same way as used for the wave packet modeling and described in Fig. 6, E(t) is the laser electric field, and $d_{n,m}$ is the transition dipole moment between the nth and mth states. The electronic structure of argon is computed as described below. The XUV absorption signals are obtained by calculating the single-atom absorption cross-section:

$$\sigma(\omega) \propto \omega \text{Im} \left[\frac{d(\omega)}{E(\omega)} \right],$$
 (B2)

where $d(\omega)$ and $E(\omega)$ are the Fourier-transformed dipole moments and applied laser field, respectively [23]. The laser electric field consists of a NIR pump pulse (750 nm, 4 fs,

TABLE V. Calculated argon Rydberg state energies.

State	Energy (eV)	
$3s^{-1}np$		
4p	26.594	
5 <i>p</i>	27.999	
6 <i>p</i>	28.513	
7p	28.761	
8p	28.901	
9p	28.987	
$3s^{-1} ns$		
4s	25.305	
5 <i>s</i>	27.630	
6 <i>s</i>	28.354	
7 <i>s</i>	28.679	
8 <i>s</i>	28.853	
9s	28.957	
$3s^{-1}$ nd		
3d	27.554	
4d	28.306	
5 <i>d</i>	28.652	
6 <i>d</i>	28.837	
7 <i>d</i>	28.947	
8d	29.018	
9 <i>d</i>	29.066	

 $5\times10^{11}\,\mathrm{W/cm^2})$ and an XUV pulse (40 nm, 80 as, $1\times10^{10}\,\mathrm{W/cm^2})$. The equation is solved by the fourth-order Runge-Kutta method at a step size of 6 as.

617

620

623

624 625

626

627

2. Oscillator strengths

The electronic structure of argon was computed by using the atomic structure calculation code of Cowan, which is based on a multiconfiguration Hartree-Fock model with empirically adjusted Slater parameters [22]. The simulation includes 20 electronic states: the ground, $3s^{-1}np$ $(4 \le n \le 9)$, $3s^{-1}ns$ $(4 \le n \le 9)$, and $3s^{-1}nd$ $(3 \le n \le 9)$ states. The state energies are given as well as the calculated oscillator strengths for the $p \to s$ and $p \to d$ transitions (see Tables V–VII).

TABLE VI. Calculated oscillator strengths, $np \rightarrow ns$.

np	4 <i>s</i>	5 <i>s</i>	6 <i>s</i>	7 <i>s</i>	8 <i>s</i>	9 <i>s</i>
4 <i>p</i>	0.35146	0.17195	0.02152	0.00785	0.00395	0.00223
5 <i>p</i>	0.00066	0.49417	0.30052	0.03288	0.01177	0.00604
6 <i>p</i>	0.00002	0.00282	0.63662	0.42942	0.04497	0.01652
7p	0.00023	0.00005	0.00551	0.77603	0.55703	0.05941
8p	0.00077	0.00015	0.00017	0.00750	0.90966	0.69965
9 <i>p</i>	0.00961	0.00556	0.00320	0.00091	0.00206	0.93299

				-						
\overline{np}	3 <i>d</i>	4 <i>d</i>	5 <i>d</i>	6 <i>d</i>	7 <i>d</i>	8 <i>d</i>	9 <i>d</i>			
${4p}$	0.16402	0.00013	0.00119	0.00124	0.00123	0.00272	0.00093			
5 <i>p</i>	0.04885	0.23818	0.00071	0.00009	0.00035	0.00135	0.00034			
6 <i>p</i>	0.00423	0.10278	0.30473	0.00284	0.00005	0.00040	0.00002			
7p	0.00173	0.00897	0.15809	0.36805	0.00562	0.00006	0.00026			
8p	0.00105	0.00342	0.01361	0.21474	0.42845	0.00673	0.00290			
9 <i>p</i>	0.00077	0.00199	0.00510	0.01827	0.27600	0.46764	0.02398			

TABLE VII. Calculated oscillator strengths, $np \rightarrow nd$.

- [1] F. Gounand, J. Phys. (Paris) 40, 457 (1979).
- [2] C. Fabre and S. Haroche, in *Rydberg States of Atoms and Molecules*, edited by R. F. Stebbings and F. B. Dunning (Cambridge Press, New York, 1983), p. 117.
- [3] H. Lefebvre-Brion and R. W. Field, *Perturbations in the Spectra of Diatomic Molecules* (Academic Press, New York, 1986).
- [4] K.-L. Pham, T. F. Gallagher, P. Pillet, S. Lepoutre, and P. Cheinet, PRX Quantum 3, 020327 (2022).
- [5] T. C. Weinacht, J. Ahn, and P. H. Bucksbaum, Nature (London) 397, 233 (1999).
- [6] P. B. Corkum and F. Krausz, Nat. Phys. 3, 381 (2007).
- [7] T. Ding, C. Ott, A. Kaldun, A. Blättermann, K. Meyer, V. Stooss, M. Rebholz, P. Birk, M. Hartmann, A. Brown *et al.*, Opt. Lett. 41, 709 (2016).
- [8] W. Cao, E. R. Warrick, A. Fidler, S. R. Leone, and D. M. Neumark, Phys. Rev. A 94, 021802(R) (2016).
- [9] W. Cao, E. R. Warrick, A. Fidler, S. R. Leone, and D. M. Neumark, Phys. Rev. A 97, 023401 (2018).
- [10] E. R. Warrick, A. P. Fidler, W. Cao, E. Bloch, D. M. Neumark, and S. R. Leone, Farad. Discuss. 212, 157 (2018).
- [11] A. P. Fidler, S. J. Camp, E. R. Warrick, E. Bloch, H. J. B. Marroux, D. M. Neumark, K. J. Schafer, M. B. Gaarde, and S. R. Leone, Nat. Commun. 10, 1384 (2019).
- [12] A. P. Fidler, H. J. B. Marroux, E. R. Warrick, E. Bloch, W. Cao, S. R. Leone, and D. M. Neumark, J. Chem. Phys. 151, 114305 (2019).
- [13] Y.-C. Lin, A. P. Fidler, A. Sandhu, R. R. Lucchese, C. W. McCurdy, S. R. Leone, and D. M. Neumark, Farad. Discuss. 228, 537 (2021).
- [14] J. D. Gaynor, A. P. Fidler, Y.-C. Lin, H.-T. Chang, M. Zuerch, D. M. Neumark, and S. R. Leone, Phys. Rev. B 103, 245140 (2021).
- [15] K. Mi, W. Cao, H. Xu, Q. Zhang, and P. Lu, Opt. Express 29, 2798 (2021).
- [16] A. P. Fidler, Y. C. Lin, J. D. Gaynor, C. W. McCurdy, S. R. Leone, R. R. Lucchese, and D. M. Neumark, Phys. Rev. A 106, 063525 (2022).
- [17] R. P. Madden, D. L. Ederer, and K. Codling, Phys. Rev. 177, 136 (1969).

- [18] M. A. Baig and M. Ohno, Z. Phys. D 3, 369 (1986).
- [19] S. L. Sorensen, T. Åberg, J. Tulkki, E. Rachlew-Källne, G. Sundström, and M. Kirm, Phys. Rev. A 50, 1218 (1994).
- [20] S. L. Wu, Z. P. Zhong, R. F. Feng, S. L. Xing, B. X. Yang, and K. Z. Xu, Phys. Rev. A 51, 4494 (1995).
- [21] H. P. Kelly and R. L. Simons, Phys. Rev. Lett. 30, 529 (1973).
- [22] R. D. Cowan, The Theory of Atomic Structure and Spectra (University of California Press, Berkeley, 1981).
- [23] M. X. Wu, S. H. Chen, S. Camp, K. J. Schafer, and M. B. Gaarde, J. Phys. B: At. Mol. Opt. Phys. 49, 062003 (2016).
- [24] X. C. Dai, E. A. Torres, E. B. W. Lerch, D. J. Wilson, and S. R. Leone, Chem. Phys. Lett. 402, 126 (2005).
- [25] H. Wang, M. Chini, S. Y. Chen, C. H. Zhang, F. He, Y. Cheng, Y. Wu, U. Thumm, and Z. H. Chang, Phys. Rev. Lett. 105, 143002 (2010).
- [26] J. Grochmalicki and M. Lewenstein, J. Phys. B: At. Mol. Opt. Phys. 21, 3285 (1988).
- [27] C. Raman, M. F. DeCamp, and P. H. Bucksbaum, Opt. Express 1, 186 (1997).
- [28] M. Y. Ivanov and A. Stolow, Chem. Phys. Lett. 265, 231 (1997).
- [29] T. C. Weinacht, J. Ahn, and P. H. Bucksbaum, Phys. Rev. Lett. 80, 5508 (1998).
- [30] V. G. Stavros and H. H. Fielding, Chem. Phys. Lett. **284**, 93 (1998).
- [31] X. C. Dai and S. R. Leone, J. Chem. Phys. **127**, 014312 (2007).
- [32] K. L. Knappenberger, E. B. W. Lerch, P. Wen, and S. R. Leone, J. Chem. Phys. 127, 124318 (2007).
- [33] H. J. B. Marroux, A. P. Fidler, D. M. Neumark, and S. R. Leone, Sci. Adv. 4, eaau3783 (2018).
- [34] A. Plunkett, M. A. Alarcón, J. K. Wood, C. H. Greene, and A. Sandhu, Phys. Rev. Lett. 128, 083001 (2022).
- [35] C. E. Moore, Atomic Energy Levels (National Bureau of Standards, Washington D.C., 1971), Vol. I, p. 91.
- [36] A. Kramida, Y. Ralchenko, and J. Reader, *NIST Atomic Spectra Database* (National Institute of Standards and Technology, Gaithersburg, 2020); https://physics.nist.gov/asd